Supporting Information

Scalable Micro-fabrication of Flexible, Solid-state, Inexpensive and High-Performance Planar Micro-supercapacitors through Inkjet Printing Method

Poonam Sundriyal[a,b] and Shantanu Bhattacharya[a,b,*]

a. Department of Mechanical Engineering, Indian Institute of Technology, Kanpur, India, 208016

b. Microsystems Fabrication Laboratory, Indian Institute of Technology, Kanpur, India, 208016

[*]Corresponding author's Email Id: bhattacs@iitk.ac.in

1. Calculation methods

1.1 Physical properties of the ink samples

The suitability of all inks for inkjet printing is determined by the Ohnesorge number (Oh). The Ohnesorge number is a dimensionless number which is related to the Reynolds number and Webber number as following:[1, 2]

Ohnesorge number (Oh): It is the ratio of square root of the Weber number and the Reynolds number.

$$\mathbf{Oh} = \frac{\sqrt{\mathbf{Weber\ number}}}{\mathbf{Reynolds\ number}} = \frac{\boldsymbol{\eta}}{\sqrt{\mathbf{a\rho\gamma}}} \quad \text{(S1)}$$

The Reynolds number and Webber number depend on the inertia, viscous and surface tension forces as follows:

Reynolds number (Re): It is the ratio of inertia to viscous forces.

$$\mathbf{Re} = \frac{\mathbf{Inertia\ force}}{\mathbf{Viscous\ force}} = \frac{\mathbf{va\rho}}{\boldsymbol{\eta}} \quad \text{(S2)}$$

Weber number (We): It is the ratio of inertia force and surface tension force.

$$\mathbf{We} = \frac{\textbf{Inertia force}}{\textbf{Surface tension}} = \frac{\mathbf{v^2 a \rho}}{\boldsymbol{\gamma}} \quad \text{(S3)}$$

Here v, a, ρ, η and γ represents average velocity, characteristic length (diameter of the printing nozzle), density, dynamic viscosity and surface tension of the ink, respectively.

1.2 Electrochemical performance

The areal capacitance (C_a) of the electrode samples and the device is evaluated from GCD curves by the following equation:

$$\mathbf{C_a} = \frac{\mathbf{i\Delta t}}{\mathbf{a\Delta V}} \quad \text{(S4)}$$

The areal capacities of the negative electrodes (AC and AC- Bi_2O_3 nanocomposite) were calculated from GCD curves by the following equation:

$$\mathbf{C_a} = \frac{\mathbf{i\Delta t}}{\mathbf{a}} \quad \text{(S5)}$$

Here, i is the constant charge/discharge current, Δt is the discharge time, a is the surface area of the electrode and ΔV is the applied potential window.

The volumetric capacitance (C_V), energy density (E_V) and power density (P_V) of planar solid-state flexible asymmetric micro-supercapacitor are calculated from the GCD curves according to the equations as follows:

$$\mathbf{C_V} = \frac{\mathbf{i\Delta t}}{\mathbf{V\Delta V}} \quad \text{(S6)}$$

$$\mathbf{E_V} = \frac{\mathbf{1}}{\mathbf{2}}\mathbf{C_V \Delta V^2} \quad \text{(S7)}$$

$$\mathbf{P_V} = \frac{\mathbf{E_V}}{\mathbf{\Delta t}} \quad \text{(S8)}$$

Here, i is the constant charge/discharge current, Δt is the discharge time, V is the total volume of the asymmetric supercapacitor (including conducting substrate, active electrode layers, and gel electrolyte, without considering the porosity effects) and ΔV is the applied potential window.

The areal capacitance (C) is calculated from the CV curves according to the following equation:

$$\mathbf{C} = \frac{\mathbf{A}}{\mathbf{2saΔV}} \quad \text{(S9)}$$

where A is the total integrated area under the CV curve, s is the scan rate, a is area of the electrode surface, and △V is the applied voltage window.

For an asymmetric supercapacitor, it is essential to balance the stored electric charge between positive and negative electrodes ($q_+ = q_-$). The stored electric charge depends on capacitance (C), voltage range (ΔV) and mass loading (m) according to the following relation:

$$\mathbf{q} = \mathbf{m} \times \mathbf{C} \times \mathbf{\Delta V} \quad \text{(S10)}$$

$$\frac{\boldsymbol{m_+}}{\boldsymbol{m_-}} = \frac{\mathbf{C_-} \times \Delta\mathbf{V_-}}{\mathbf{C_+} \times \Delta\mathbf{V_+}} \quad \text{(S11)}$$

Here, m_+ and m_- are masses of active materials on positive and negative electrodes, respectively.

For a printed device the mass of active material depends on the number of printing layers and capacitance continuously changes with the number of printing layers. Therefore, instead of mass, we balanced the stored charge with the printing layers (graphically represented in result and discussion part) according to the following equation:

$$\frac{L_+}{L_-} = \frac{C_- \times \Delta V_-}{C_+ \times \Delta V_+} \quad \text{(S12)}$$

Here, L_+ and L_- are the number of printing layers on positive and negative electrodes.

2. Experimental

2.1 Preparation of the GO ink

Graphene oxide (GO) was fabricated from graphite flakes according to the modified Hummers method.[3, 4] The as-prepared GO sheets were exfoliated in DI water by ultrasonication for 1 h. Meanwhile, the EG and ethanol were slowly added to the mixture solution. The obtained solution shows no sedimentation of GO sheets after centrifuging at 2000 rpm for 15 min, which indicates complete exfoliation and well dispersion of GO sheets in the solution. This solution was stable for a long time (>200 days). Further, the particle sizes of the GO sheets were reduced using probe sonication and filtered with a 450 nm syringe filter to separate the large sized sheets. The obtained solution of reduced graphene oxide (rGO) was used for further processing.

2.2 Preparation of the rGO- MnO_2 nanocomposite ink

The MnO_2 nanostructures were synthesized by adding 0.05 M $KMnO_4$ into 0.2 M HCl solution. The mixed solution was transferred to a Teflon-line autoclave and maintained at 150° C for 1 h. The hydrothermal reaction leads to the formation of MnO_2 nanostructures, which were washed with DI water and collected by filtration. The prepared MnO_2 nanostructures were further dried at 120° C for 6 hr. Further, the MnO_2 nanostructures were dispersed in the water and water- EG-ethanol solutions using stirring and sonication. However, the obtained dispersion was unstable with rapid precipitation in the water-based ink solution. Therefore the MnO_2 nanostructures were further mixed with the already prepared GO ink solution (GO: MnO_2= 1:1). This mixture was stirred for 30 min followed by sonication for 45 min. The prepared mixture solution was termed as rGO-MnO_2 nanocomposite ink.

2.3 Preparation of the AC- Bi_2O_3 nanocomposite ink

The AC ink was prepared by dispersing conducting AC powder in the water- EG- ethanol solution. Initially, AC powder was sonicated by 30 min of bath sonication and 45 min of probe sonication. The large sized particles were separated by filtering the mixed solution using a 250 µm syringe filter. The AC-Bi_2O_3 nanocomposite was prepared by a solvothermal method with some modifications in previous literature, [5] which was further converted to a printable ink. In a typical method, 0.8 g of $Bi(NO_3)_3.5H_2O$ was dissolved in a mixed solution of 30 mL of ethanol and 15 mL of EG. It was stirred for 60 min and simultaneously already prepared AC ink (0.8 g in 10 mL) was mixed in it. The mixture solution was transferred into a Teflon-lined stainless steel autoclave and heated to 160° C for 8 h. After the room temperature cooling of the autoclave, the collected nanocomposite was washed with ethanol and DI water and dried at 80° C for 6 h. The dried AC- Bi_2O_3 nanocomposite was further mixed with water-EG-ethanol mixture solution using sonication. The developed ink was stable with good dispersion of nanocomposite particles in the ink solution. Bi_2O_3 nanostructures were also prepared following the same procedure without adding AC in it.

2.4 Preparation of PVA- KOH electrolyte ink

The PVA- KOH electrolyte ink was prepared by mixing 6M KOH and PVA (4g) in 100 mL of DI water with continuous stirring at 85° C for 2 hr. The obtained solution was filtered using a 450 nm syringe filter, and the freshly prepared solution was used as an electrolyte ink.

2.5 Inkjet printing of prepared inks on cellulose paper substrate and device fabrication

All the components of the SC device including; conducting layer, electrode layers, and the electrolyte were printed on the cellulose paper substrates using an EPSON L130 desktop inkjet printer. The physical properties of all inks were carefully optimized before filling them in the ink cartridge. Printing was performed in the high- quality and low- speed mode to achieve the best print quality of the printed patterns. Initially, digitally designed patterns were printed on different paper substrates using GO ink and reduced with the hydrazine hydrate. The rGO printed paper substrates were annealed for 24 h at 90° C and then checked for the comparative change in the electrical resistance values. Out of the different cellulose papers such as bond paper, A4 paper, photo paper, and glossy paper, the bond paper shows the best conductivity. Therefore, it was used as a substrate for flexible SCs.

Further, all the electrode material's inks (MnO_2, rGO-MnO_2, AC, and AC-Bi_2O_3) were printed on the already printed reduced graphene oxide conducting paper (RGCP) substrate at the separate locations of paper to make individual electrodes. These electrodes were first studied in the 6 M KOH electrolyte. The electric charge was balanced between the positive and negative electrodes before fabrication of an asymmetric supercapacitor device. Further, the planar micro-supercapacitor with interdigitated patterns were fabricated by the simultaneous printing of rGO-MnO_2 ink patterns as the positive electrode and AC-Bi_2O_3 ink patterns as the negative electrode over the RGCP patterns (as illustrated in Fig. 1 of the main manuscript). Further, the PVA-KOH ink was printed over the pre-patterned positive and negative electrode to form a planar micro-supercapacitor device. This fully inkjet-printed planar micro-supercapacitor was dried at 45° C for 24 h to ensure the complete solidification of the electrolyte gel. Finally, the full inkjet printed, planar, and asymmetric micro-supercapacitor (PAμSC) with electrodes- electrolyte assembly was sealed with a parafilm foil and encapsulated by a thin PDMS layer to prevent the dehydration of the gel electrolyte.

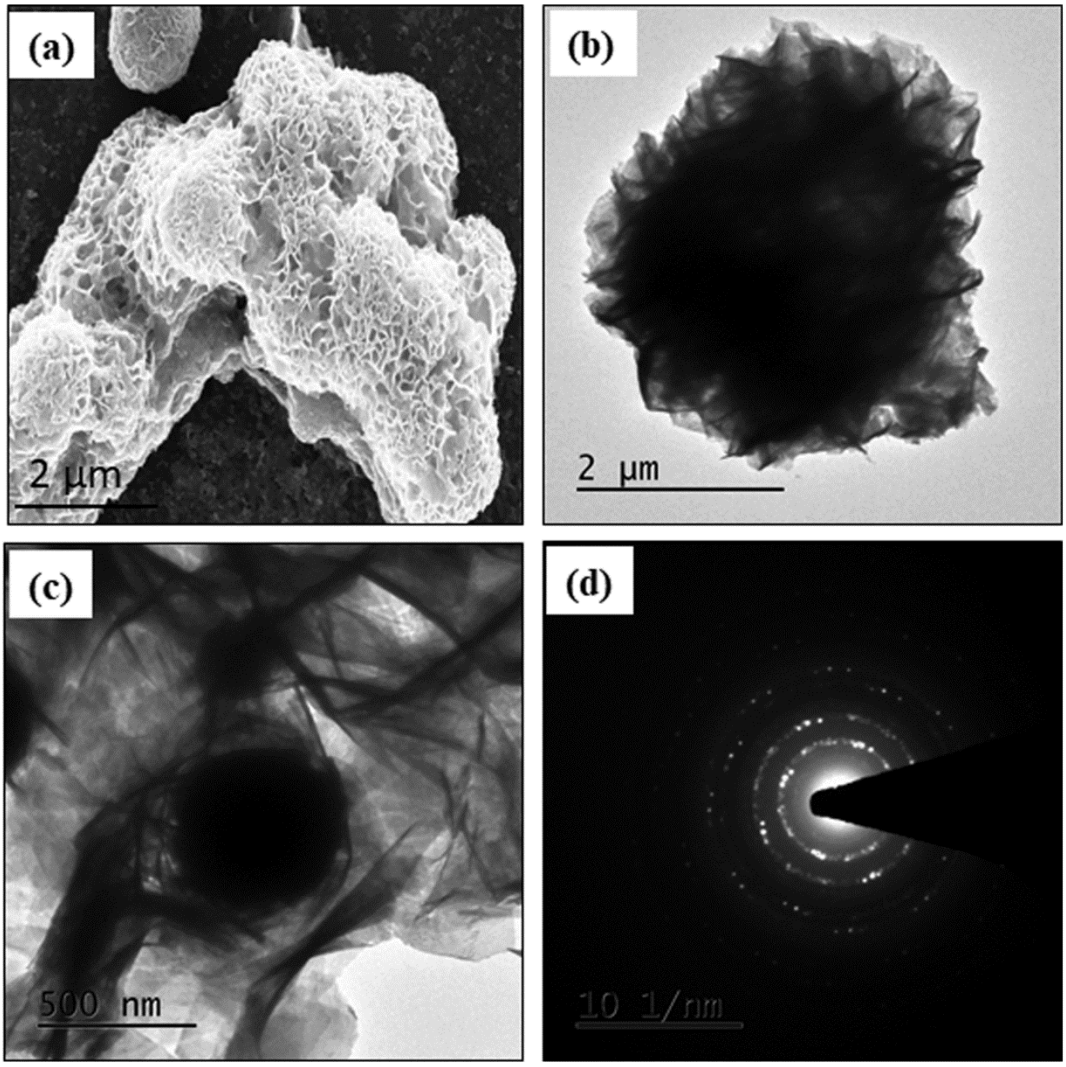

Fig. S1 (a) The SEM image of AC- Bi_2O_3 nanocomposite, (b) TEM image of the Bi_2O_3, (c) TEM image of the AC-Bi_2O_3 nanocomposite, and (d) SAED pattern of the Bi_2O_3.

3. Material characterization of the Positive Electrode

The rGO-MnO_2 nanocomposite electrode was chosen as the positive electrode of the asymmetric micro- supercapacitor (AμSC). Fig. S2 a shows XRD patterns of the rGO, MnO_2, and rGO-MnO_2 nanocomposite materials. The XRD peaks of MnO_2 and rGO- MnO_2 nanocomposite matches well with the cubic phase δ-MnO_2 (JCPDS card no. 80-1098).[6] Further, a distinct peak at 652 cm^{-1} in the RAMAN spectra of rGO- MnO_2 nanocomposite sample (Fig. S2 Fig. b) confirms the presence of MnO_2 in the nanocomposite. In addition, the integrated intensity ratio of the D and G bands (I_D/ I_G) of rGO and rGO- MnO_2 nanocomposite were calculated to be 1.006 and 1.616, respectively. This major shift in the intensity ratio indicates the emergence of structural disorders in the graphene due to the presence of MnO_2 in the graphene layers.[7, 8]

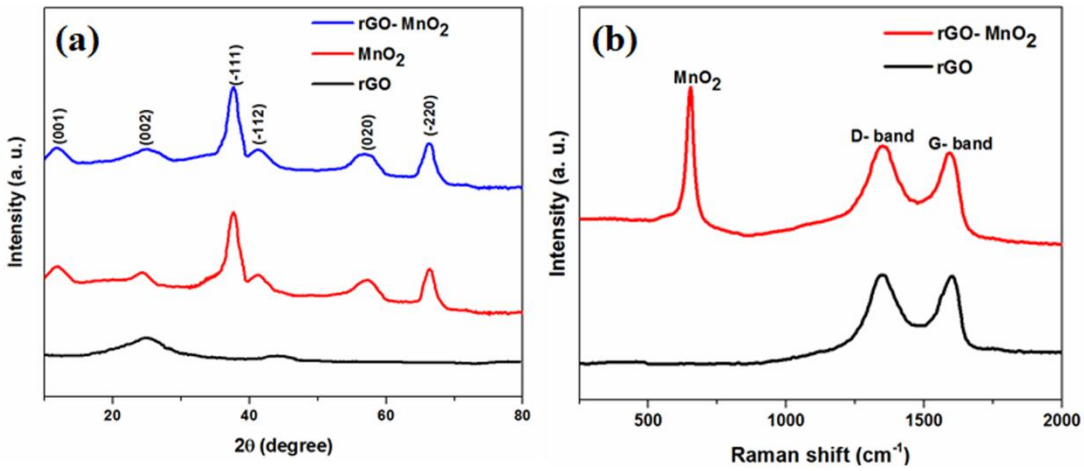

Fig. S2 (a) XRD patterns of rGO, MnO_2, and rGO- MnO_2 nanocomposite, and (b) XRD spectra of rGO and rGO- MnO_2 nanocomposite.

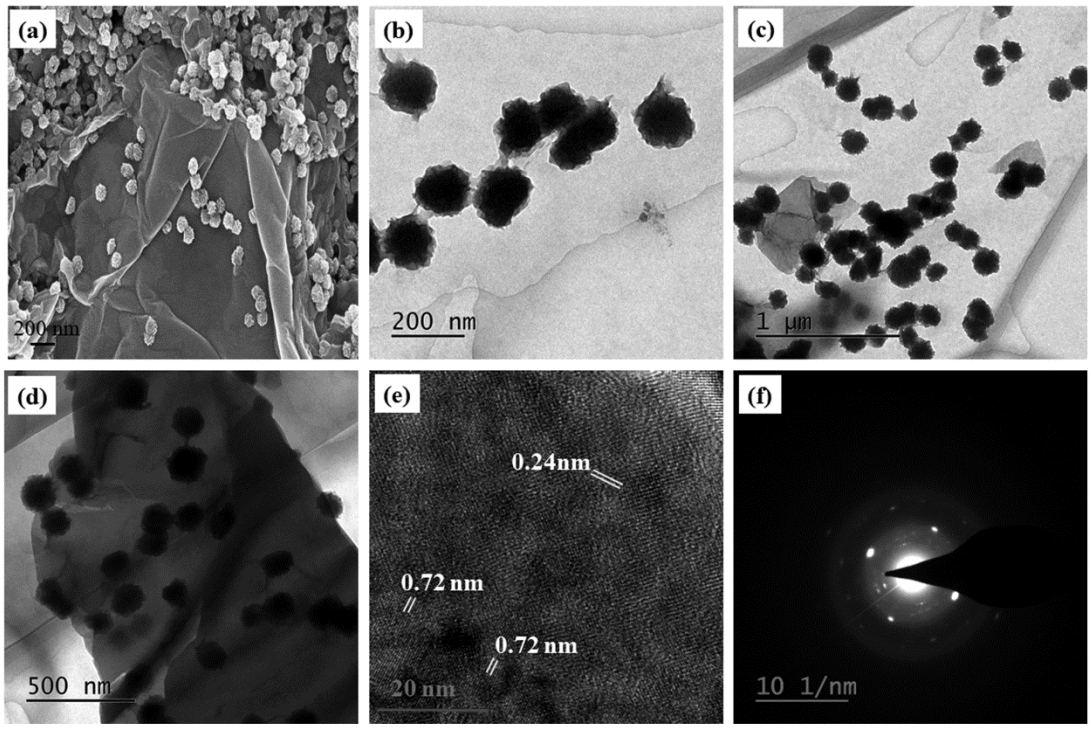

Fig. S3 (a) SEM and (b- d) TEM image of the rGO-MnO_2 nanocomposite, (e) HRTEM image of MnO_2, and (f) SAED pattern of the rGO-MnO_2 nanocomposite.

SEM images of the rGO-MnO_2 nanocomposite (Fig. S3 a) shows the well spread MnO_2 nanostructures on the crumbled rGO sheets. The combined effect of the MnO_2 nanostructures and rGO sheets can effectively improve the conductivity and energy storage capacity of the nanocomposite material. The rGO-MnO_2 nanocomposite was further investigated by TEM. Fig. S3 b-d distinctively reveals well dispersion of MnO_2 nanostructures on rGO sheets. The calculated lattice spacings from high-resolution TEM (HRTEM) image of the nanocomposite (Fig. S3 e) are 0.72 nm and 0.24 nm, which are related to the (001) and (11-1) planes of the δ-MnO_2. The selected area electron diffraction (SAED) pattern (Fig. S3 f) shows the dispersed rings, indicating the polycrystalline nature of the nanocomposite. TEM images of the MnO_2 nanostructures, the rGO sheets and other SEM and TEM images of rGO- MnO_2 nanocomposite are displayed in Fig. S4.

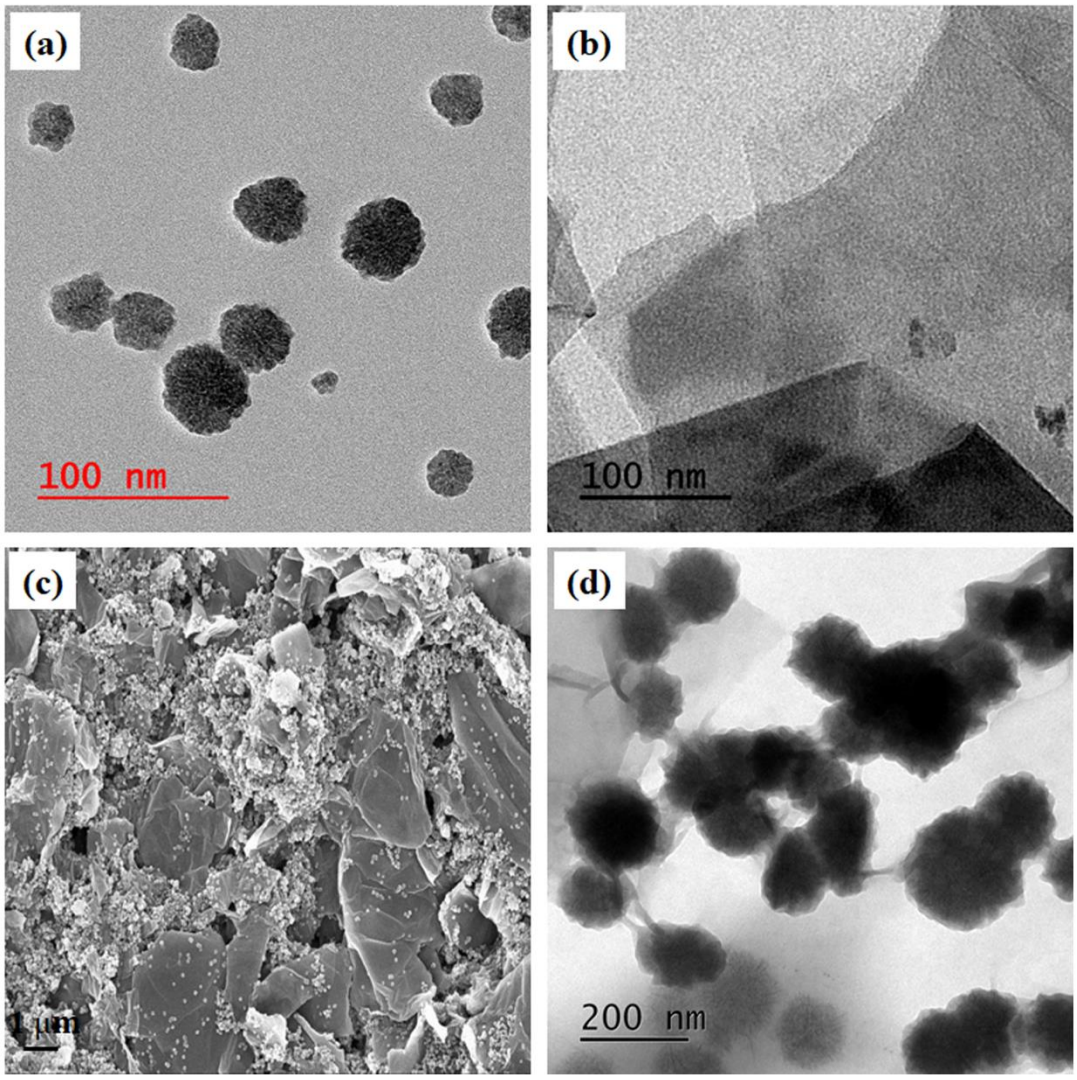

Fig. S4 TEM image of (a) MnO_2, (b) GO sheets, (c) SEM image of the rGO-MnO_2 nanocomposite, and (d) TEM image of the rGO-MnO_2 nanocomposite.

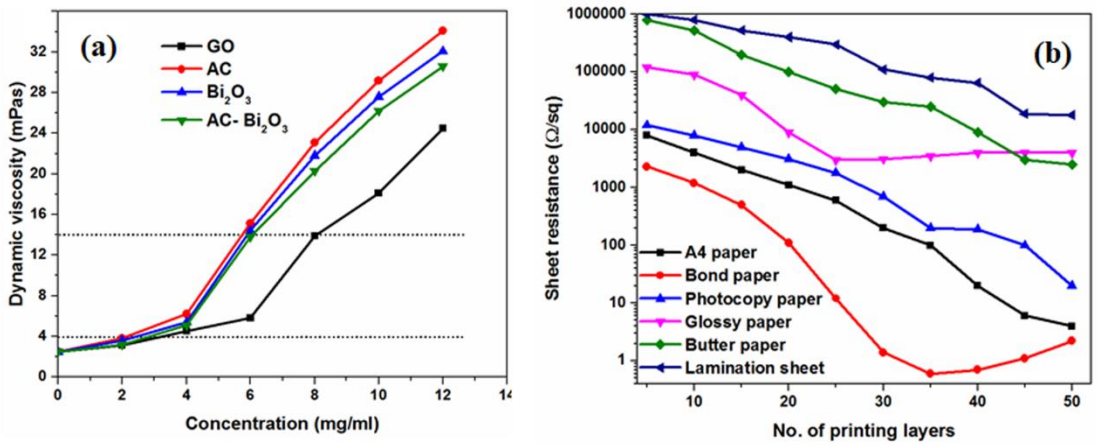

Fig. S5. Comparison of: (a) Viscosity vs. concentration for GO, AC, Bi_2O_3, and AC- Bi_2O_3 nanocomposite inks (at a shear rate of 200 s^{-1} and 25 °C temperature), and (b) Sheet resistance of different substrates with different printing passes.

Table S1. Physical properties of all inks

S. No.	Ink composition	Density (Kg/m^3)	Viscosity (mPa-s)	Surface tension (mN/m)	Inverse Ohnesorge number (Z)
1.	GO (in water+ EG+ ethanol)	1080	5.8	51	5.72
2.	AC (in water+ EG+ ethanol)	1180	6.2	56	5.86
3.	Bi_2O_3 (in water+ EG+ ethanol)	1105	5.4	55	6.46
4.	AC- Bi_2O_3 (in water+ EG+ ethanol)	1120	5.1	54	6.81
5.	MnO_2 (in water+ EG+ ethanol)	1160	6.2	56	5.81
6.	rGO- MnO_2 (in water+ EG+ ethanol)	1140	5.8	57	6.22
7.	PVA- KOH (in water)	2100	9.1	61	5.56

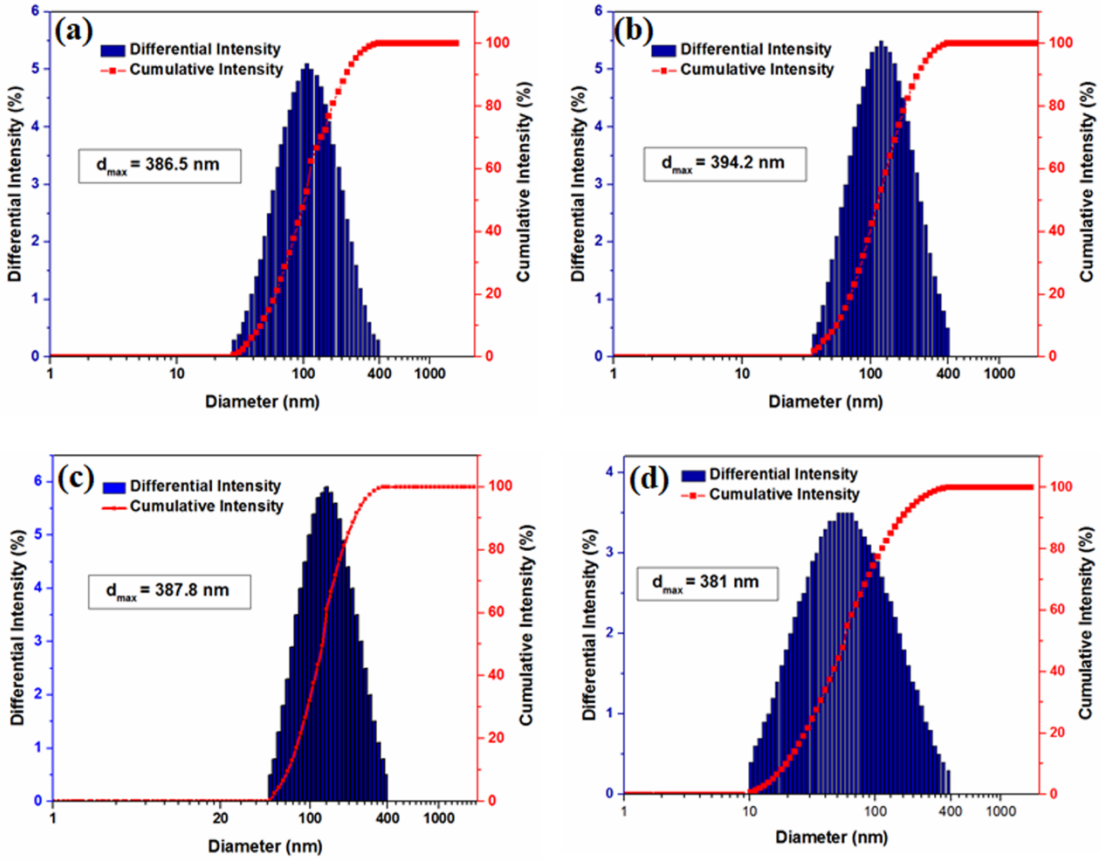

Fig. S6. DLS results of (a) GO ink, (b) AC ink, (c) AC- Bi_2O_3 composite ink and (d) PVA-KOH electrolyte ink.

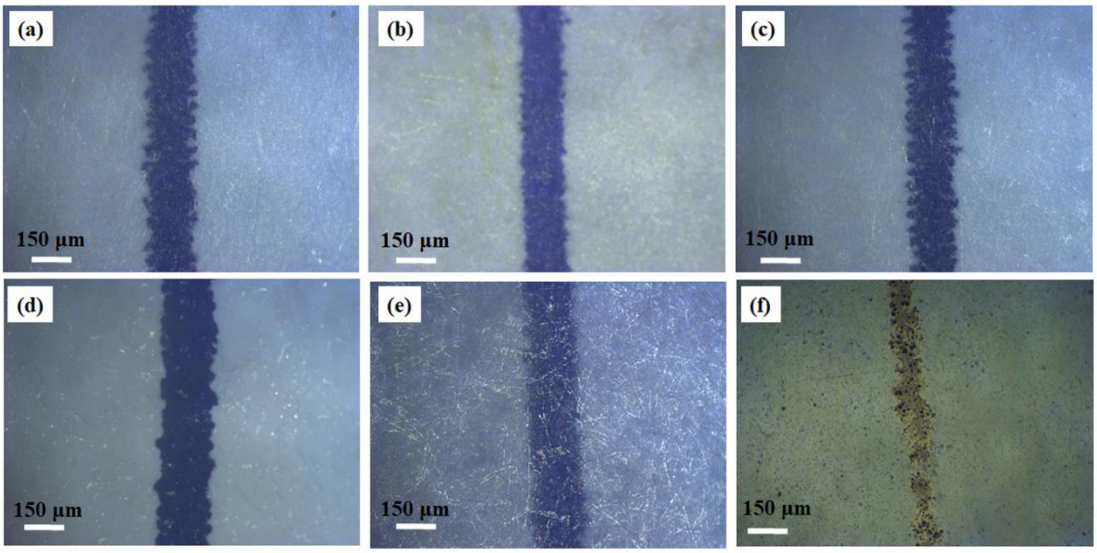

Fig. S7. Optical images of the printed line on different substrates: (a) A4 paper, (b) Bond paper, (c) Photo paper, (d) Glossy paper, (e) Butter paper, and (f) Lamination sheet.

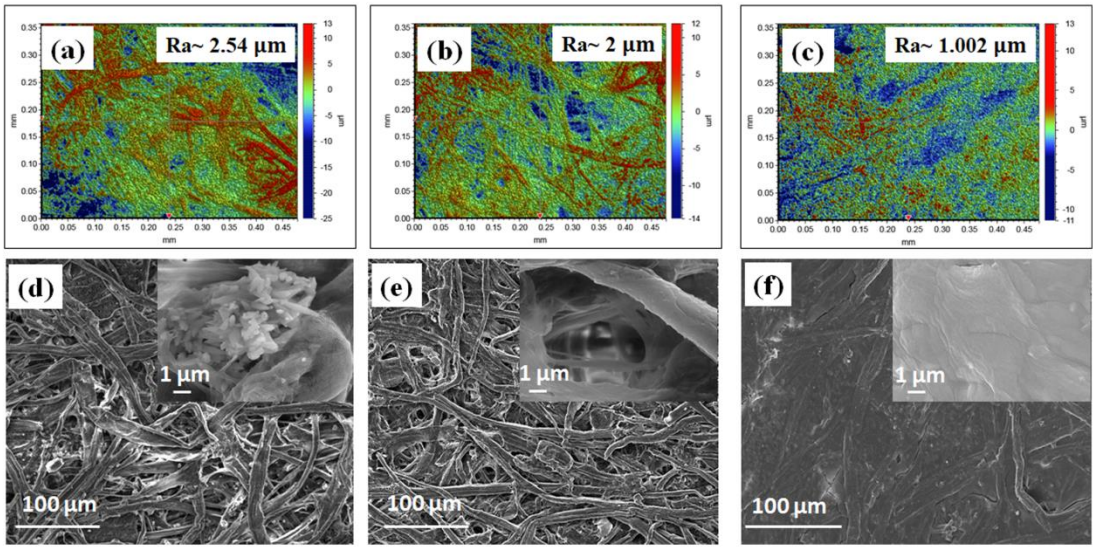

Fig. S8. 3D optical profilometry images of the bond paper: (a) as obtained; (b) after HCl treatment; (c) after rGO printing, and FESEM images of the bond paper: (d) as obtained; (e) after HCl treatment; (f) after rGO printing.

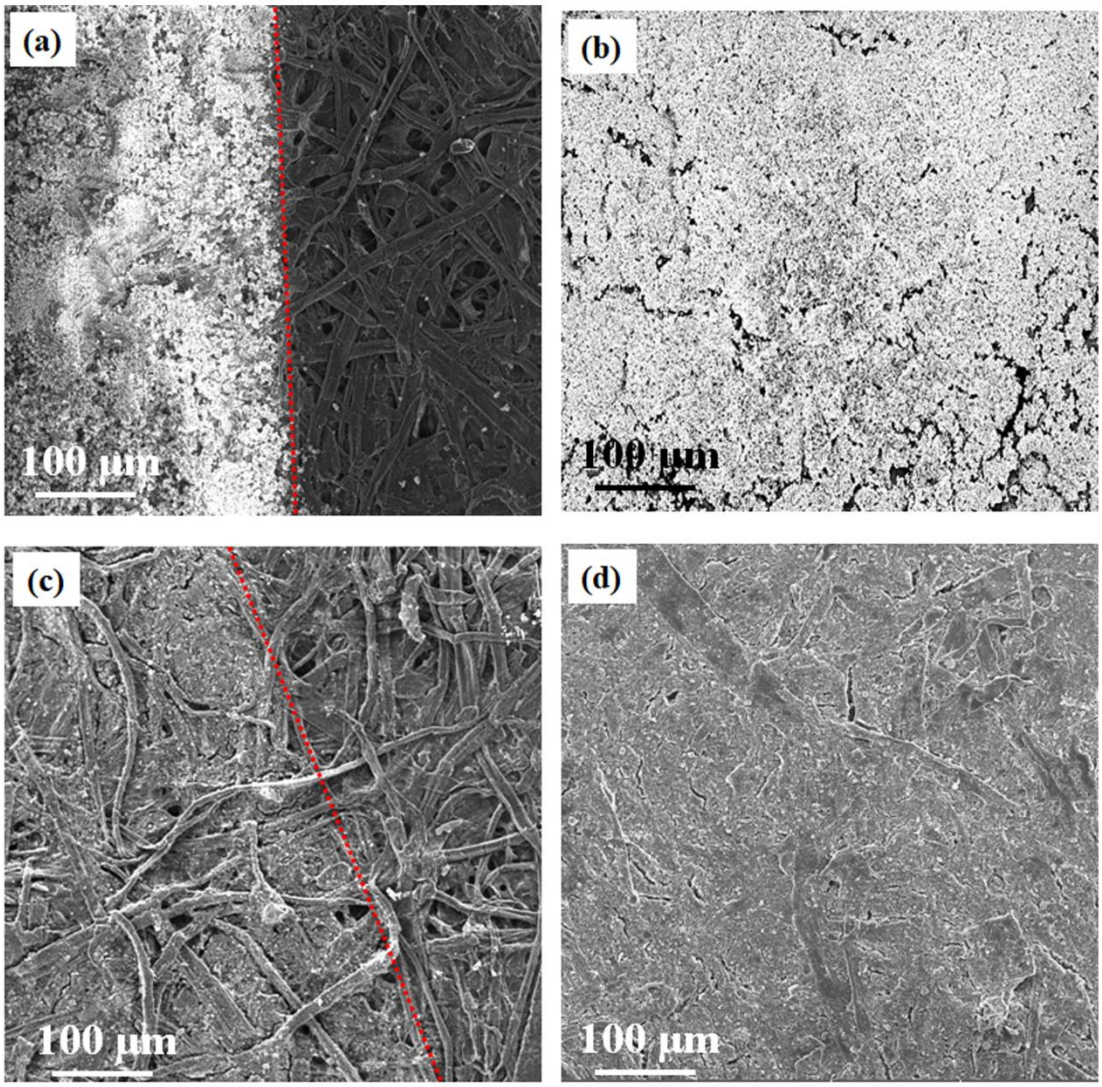

Fig. S9. FESEM images of the printed patterns with (a and b) AC- Bi_2O_3 ink, and (c and d) rGO-MnO_2 ink.

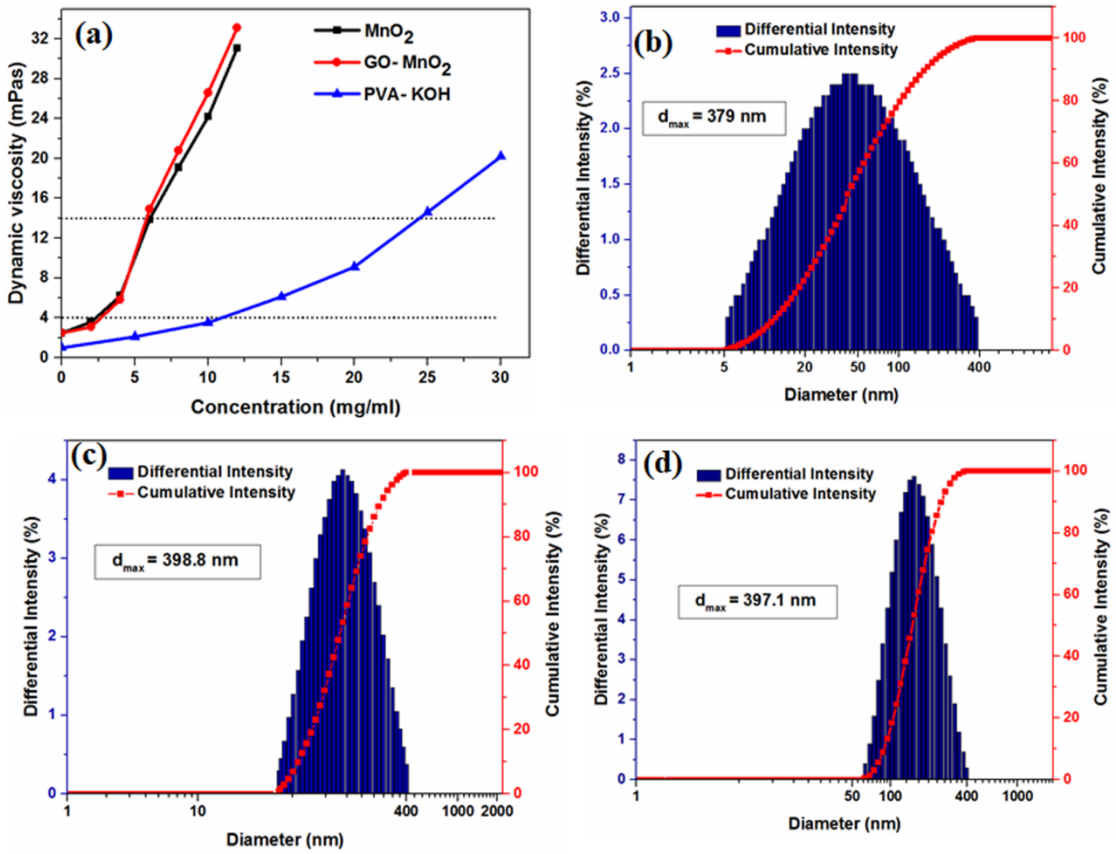

Fig. S10. (a) Viscosity vs. concentration for MnO_2, rGO-MnO_2, and PVA-KOH electrolyte inks (at a shear rate of 200 s^{-1} and 25 °C temperature), DLS results of (b) MnO_2 ink, (c) rGO-MnO_2 composite ink and (d) PVA-KOH electrolyte ink.

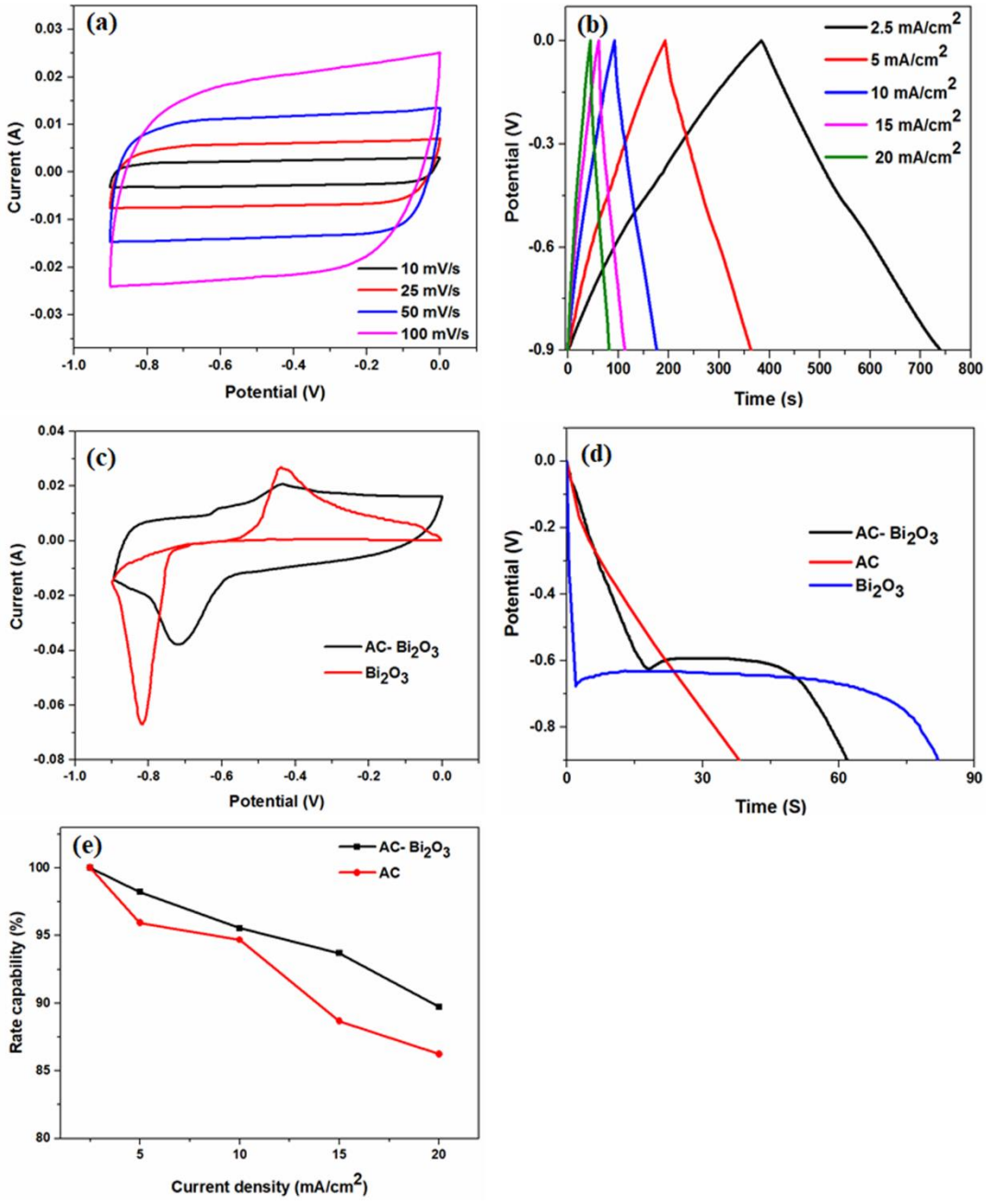

Fig. S11 (a) CV curves of the AC at various scan rates, (b) GCD curves of AC at different current densities, (c) Comparison of CV profiles of Bi_2O_3 and AC- Bi_2O_3 nanocomposite at a scan rate of 25 mV/s, (d) Comparison of discharge curves of Bi_2O_3, AC, and AC- Bi_2O_3 nanocomposite at a fixed current density of 20 mA/cm^2, and (e) Comparison of rate capability of AC and AC- Bi_2O_3 nanocomposite at various current densities.

4. Electrochemical performance of the Positive Electrode

The charge storage mechanism related to the MnO_2 based electrode materials includes either absorption/desorption or intercalation/de-intercalation of the cations /protons (such as K^+, Na^+, Li^+,etc.). These mechanisms are well explained in the previous literature.[9] δ- MnO_2 phase exhibits co-existence of both the processes with the predominance of surface adsorption/ desorption process and exhibits a rectangular voltammogram.[9, 10]

The electrochemical performance of the positive electrodes was investigated in a three-electrode system in 6M KOH aqueous electrolyte within a voltage window of 0 to 0.9 V. The comparative CV curves (Fig. S12 a) of the RGCP, MnO_2, and rGO- MnO_2 nanocomposite at 25 mV/s scan rate demonstrates a higher capacitance of rGO- MnO_2 nanocomposite as compared to the MnO_2. This result validates that the addition of rGO with MnO_2 nanostructures provides a significant gain in terms of capacitance. These curves also affirm less background effect due to RGCP. The CV curves of the rGO-MnO_2 nanocomposite at different scan rates as shown in Fig. S12 b displays near rectangular shape with mirror-image symmetry which indicates the ideal capacitive behavior. In addition, the triangularly shaped GCD curves of the rGO-MnO_2 nanocomposite at different current densities (Fig. S12 c) shows near-linear discharge profiles with the negligible resistive drop, which again illustrates the excellent electrochemical performance of the electrodes. According to the eq S4, the maximum areal capacitance achieved for rGO- MnO_2 nanocomposite was 1.361 F/cm^2 at 2.5 mA/cm^2 current density.

Fig. S12 d shows a comparison of areal capacitance and rate capability of the rGO- MnO_2 nanocomposite with different current densities. The printed nanocomposite electrode exhibit excellent rate capability, with 94.7 % capacitance retention as the current density increases from 2.5 to 20 mA/cm^2. These values are much higher than the previously reported literature in the area of MnO_2 based nanocomposite electrodes.[11-14] The improved rate capability and electrochemical performance of the rGO- MnO_2 nanocomposite electrode is due to the increased conductivity, high active surface area, fast electron transfer and short ion diffusion path. Well-dispersed MnO2 nanostructures in between the highly conducting rGO scaffold layers effectively prevent restacking of rGO layers and maintain its good conducting properties. Thus, the collective benefits of conducting rGO and MnO_2 nanostructures promote the efficient electrochemical performance of the nanocomposite electrodes. As the printed rGO- MnO_2 nanocomposite electrode exhibits excellent rate capability, high areal capacitance and a stable window between 0 to 0.9 V, it could be an excellent positive electrode to construct an asymmetric supercapacitor device.

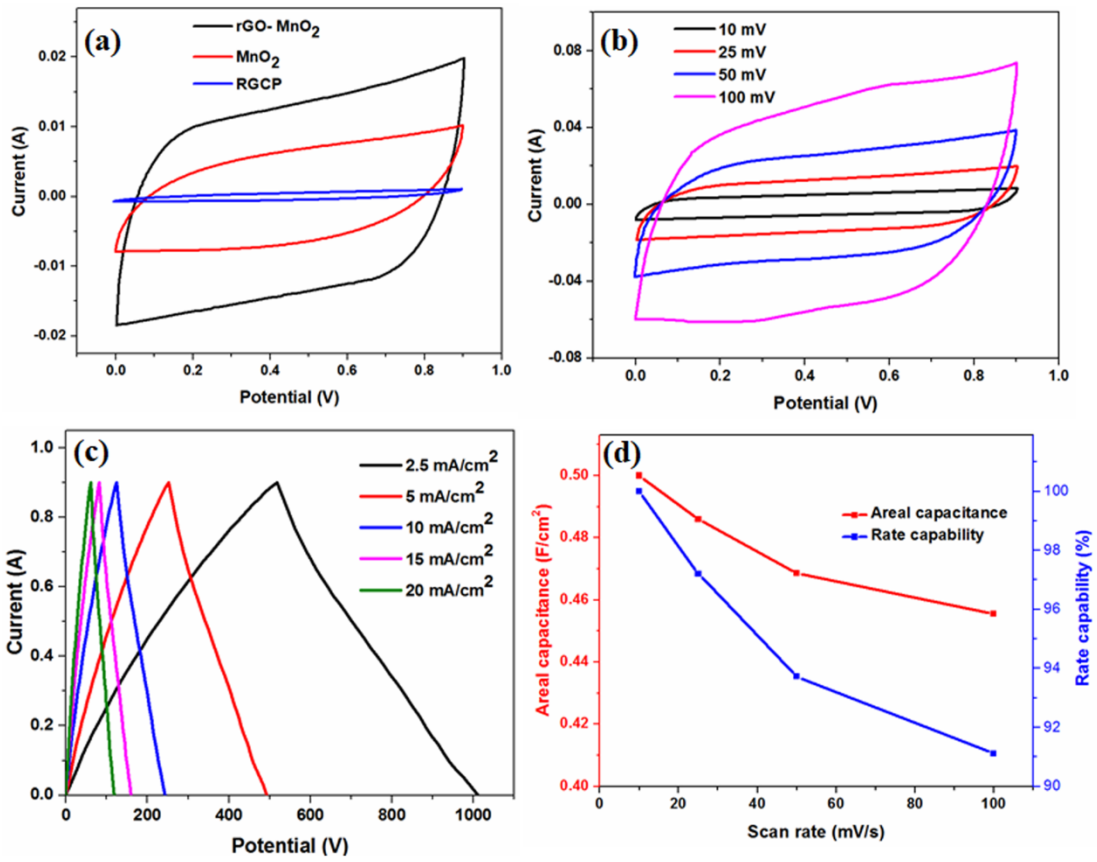

Fig. S12 (a) Comparison of CV curves of RGCP, MnO_2, and rGO- MnO_2 nanocomposite electrodes at a scan rate of 25 mV/s, (b) CV curves of rGO- MnO_2 nanocomposite at various scan rates, (c) GCD curves of rGO- MnO_2 nanocomposite at different current densities, and (d) Variation of areal capacitance and rate capability of rGO- MnO_2 nanocomposite at various current densities.

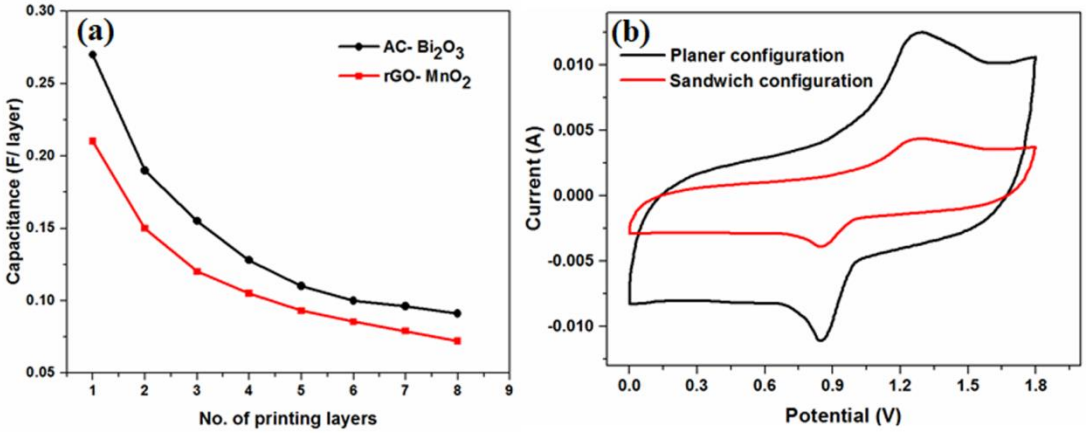

Fig. S13 (a) Variation of the capacitance of AC- Bi_2O_3 and rGO- MnO_2 electrodes with number of printing layers, and (b) Comparison of CV curves of AC- Bi_2O_3// rGO- MnO_2 SCs with in-plane and sandwich configurations in a voltage range of 0 to 1.8 V (at 25 mV/s scan rate).

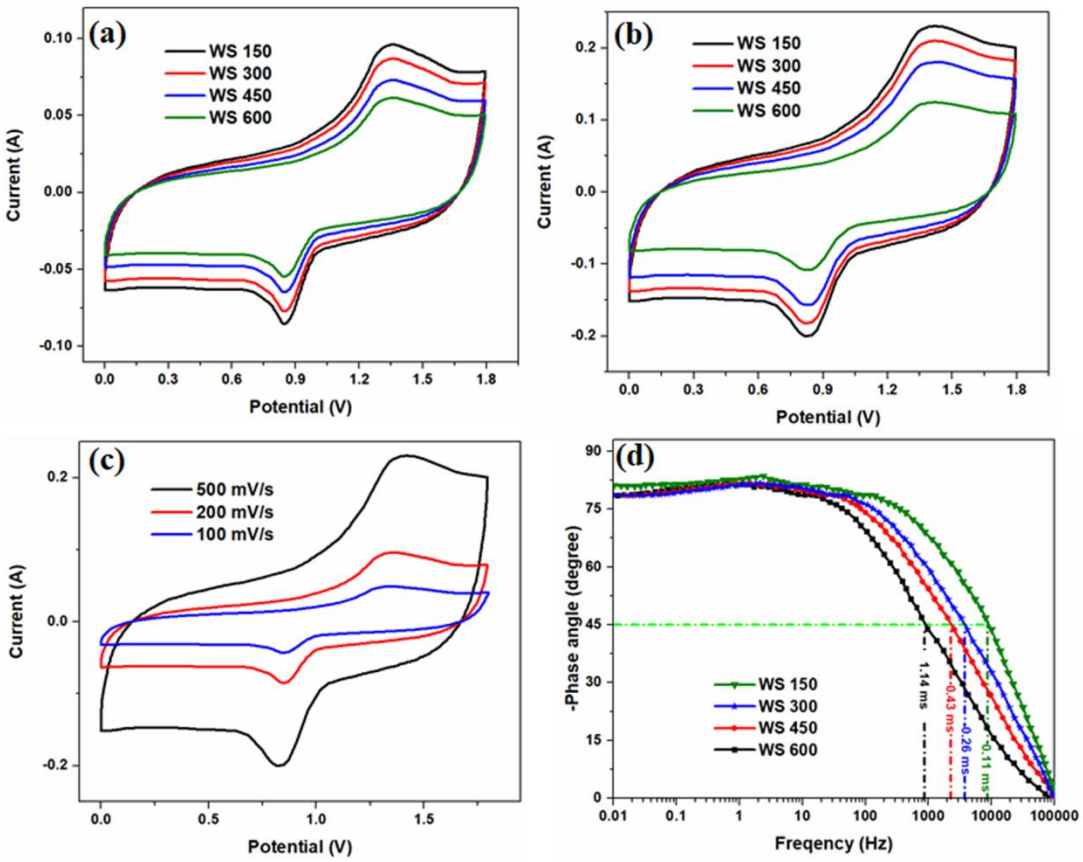

Fig. S14 Comparison of the CV curves of the PAμSCs with different width of the interspace (WS150, WS 300, WS 450, and WS 600) between the adjacent fingers at different scan rates (a) 200 mV/s, (b) 500 mV/s, (c) Comparison of the CV curves of the PAμSC WS 150 at different scan rates, and (d) Bode plots in the frequency range of 0.01 Hz to 100 kHz. The frequencies corresponding to the 45° phase angle shows the power capabilities of the different PAμSCs.

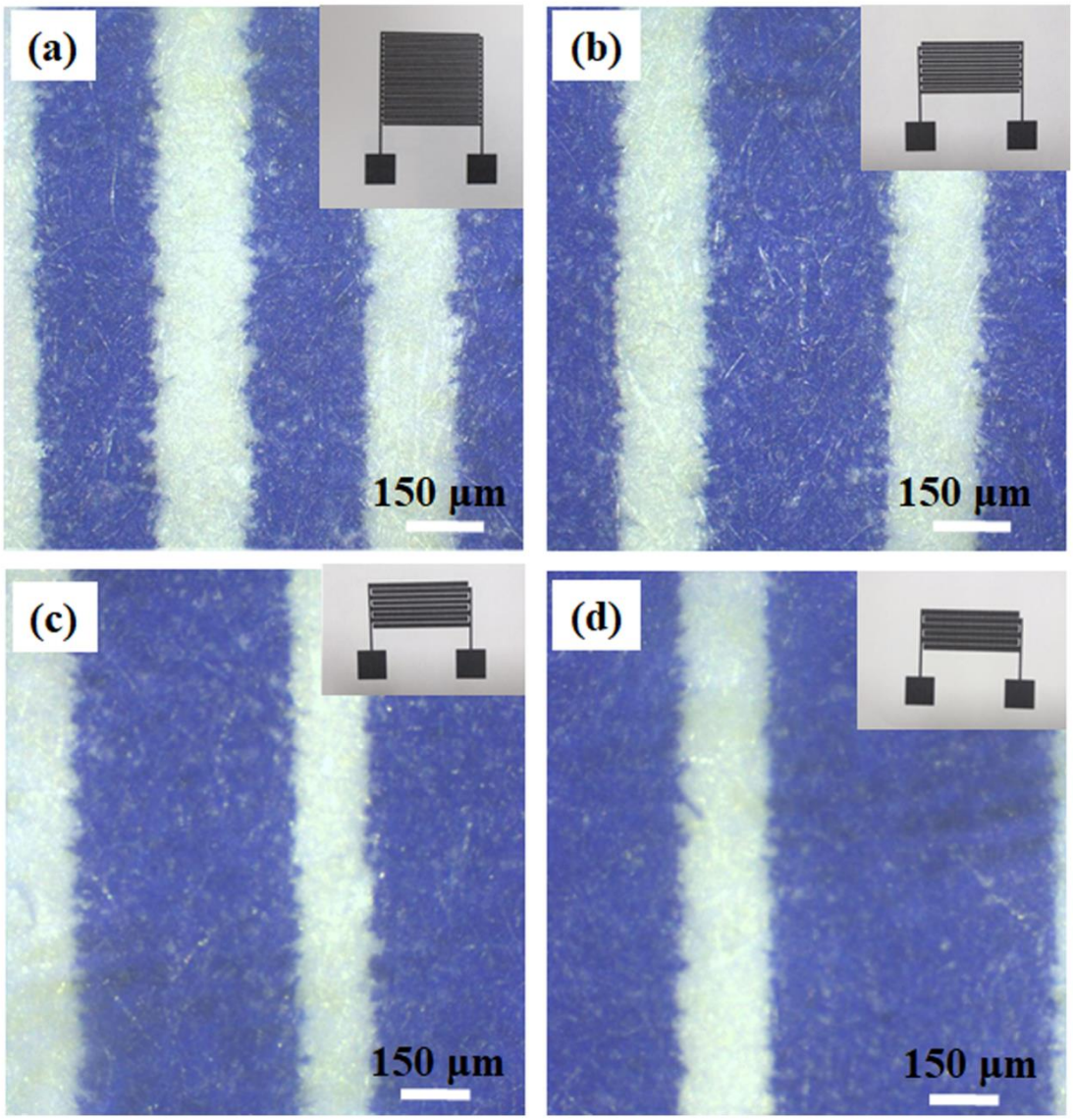

Fig. S15 Optical images of the electrode patterns of µASCs with different width of the electrode fingers: (a) 150 µm, (b) 300 µm, (c) 450 µm, and (d) 600 µm. (inset images display the digital photograph of the corresponding electrode pattern)

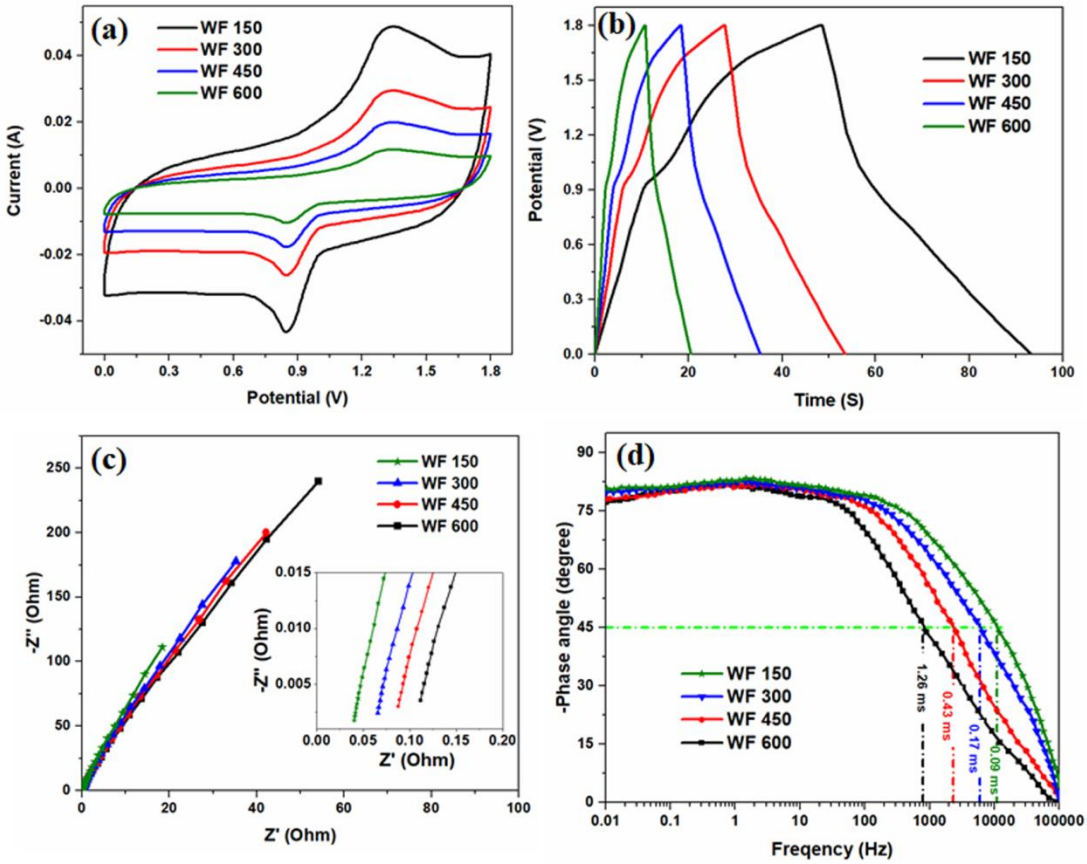

Fig. S16 Electrochemical performance of PAμSC with different width of the electrode fingers (WF 150, WF 300, WF 450, and WF 600) between the adjacent fingers: (a) Comparison of the CV curves of the MSCs at a scan rate of 100 mV/s, (b) Comparison of the GCD curves of the MSCs at a fixed current density of 20 mA/cm^2, (c) Nyquist plots of the different MSCs (inset is the magnified plot of the high- frequency region), and (d) Bode plots in the frequency range of 0.01 Hz to 100 kHz. The frequencies corresponding to the 45° phase angle shows the power capabilities of the different PAμSCs.

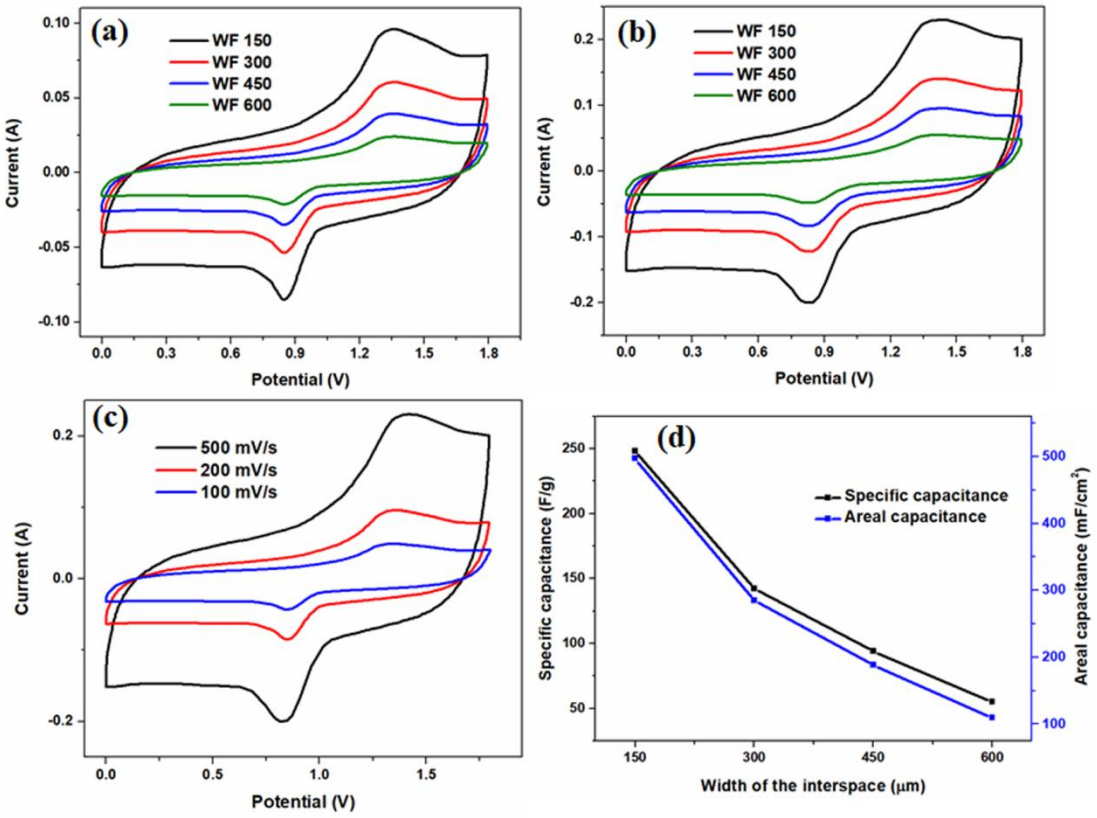

Fig. S17 Comparison of the CV curves of the PAμSCs with different width of the electrode fingers (WF 150, WF 300, WF 450, and WF 600) at different scan rates (a) 200 mV/s, (b) 500 mV/s, (c) Comparison of the CV curves of the MSC WF 150 at different scan rates, and (d) Variation of the areal capacitance with different width of the electrode fingers at a fixed current density of 20 mA/cm^2.

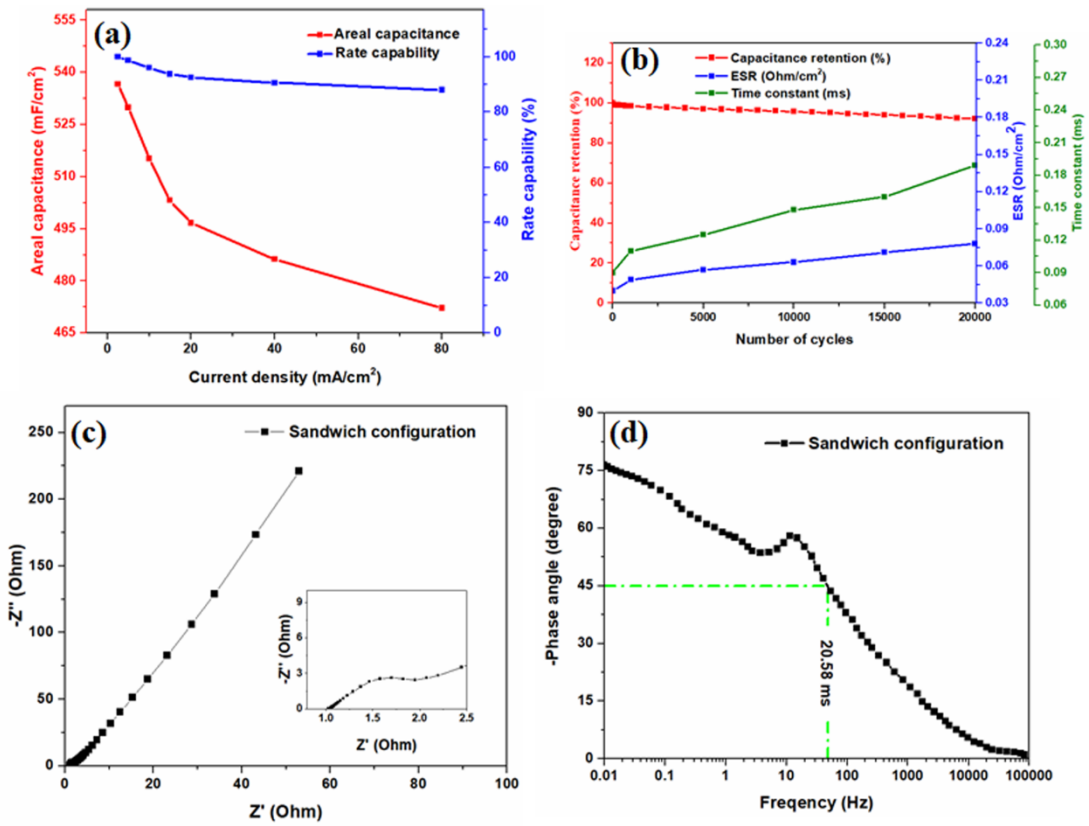

Fig. S18 (a) Variation of the areal capacitance and rate capability of the optimized AC-Bi_2O_3// rGO-MnO_2 PAμSCs device at different current densities, (b) Variation in the capacity retention, ESR and time constant of the optimized AC-Bi_2O_3// rGO-MnO_2 PAμSCs device with different charge/ discharge cycles, (c) Nyquist plot, and (d) Bode plot for the sandwich configuration.

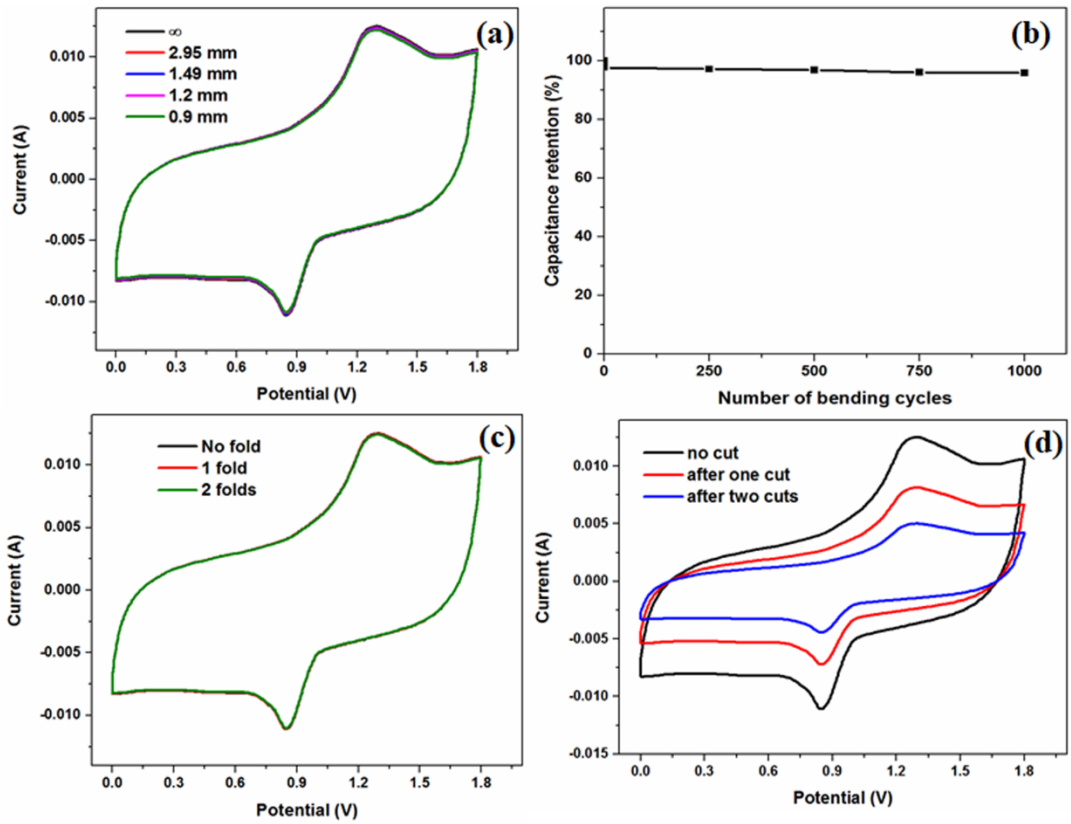

Figure S19. (a) CV profiles of the PAμSC device at different bending radii. (b) Capacity retention after various bending cycles at 0.9 mm radius. (c) Comparative CV curves of PAμSC device at different number of folds, and (d) Variation in the CV curves of PAμSC device at different number of cuts.

References

(1) Fromm, J., Numerical calculation of the fluid dynamics of drop-on-demand jets. *IBM J. Res. Dev.* **1984,** *28*, 322-333.

(2) Jang, D.; Kim, D.; Moon, J., Influence of fluid physical properties on ink-jet printability. *Langmuir* **2009,** *25*, 2629-2635.

(3) Hummers Jr, W. S.; Offeman, R. E., Preparation of graphitic oxide. *J. Am. Chem. Soc.* **1958,** *80*, 1339-1339.

(4) Marcano, D. C.; Kosynkin, D. V.; Berlin, J. M.; Sinitskii, A.; Sun, Z.; Slesarev, A.; Alemany, L. B.; Lu, W.; Tour, J. M., Improved synthesis of graphene oxide. *ACS Nano* **2010,** *4*, 4806-4814.

(5) Xu, H.; Hu, X.; Yang, H.; Sun, Y.; Hu, C.; Huang, Y., Flexible Asymmetric Micro-Supercapacitors Based on Bi_2O_3 and MnO_2 Nanoflowers: Larger Areal Mass Promises Higher Energy Density. *Adv. Energy Mater.* **2015,** *5*.

(6) Li, F.; Xing, Y.; Huang, M.; Li, K. L.; Yu, T. T.; Zhang, Y. X.; Losic, D., MnO_2 nanostructures with three-dimensional (3D) morphology replicated from diatoms for high-performance supercapacitors. *J. Mater. Chem. A* **2015,** *3*, 7855-7861.

(7) Yan, J.; Fan, Z.; Wei, T.; Qian, W.; Zhang, M.; Wei, F., Fast and reversible surface redox reaction of graphene–MnO_2 composites as supercapacitor electrodes. *Carbon* **2010,** *48*, 3825-3833.

(8) Basu, A.K.; Chauhan, P. S.; Awasthi, M.; Bhattacharya, S., α-Fe2O3 loaded rGO nanosheets based fast response/recovery CO gas sensor at room temperature. *Appl. Surf. Sci.* **2019**, *465*, 56-66.

(9) Bag, S.; Raj, C. R., Facile shape-controlled growth of hierarchical mesoporous δ-MnO_2 for the development of asymmetric supercapacitors. *J. Mater. Chem. A* **2016,** *4*, 8384-8394.

(10) Toupin, M.; Brousse, T.; Belanger, D., Charge storage mechanism of MnO_2 electrode used in aqueous electrochemical capacitor. *Chem. Mater.* **2004,** *16*, 3184-3190.

(11) Zhang, J.; Yang, X.; He, Y.; Bai, Y.; Kang, L.; Xu, H.; Shi, F.; Lei, Z.; Liu, Z.-H., δ-MnO_2 /holey graphene hybrid fiber for all-solid-state supercapacitor. *J. Mater. Chem. A* **2016,** *4*, 9088-9096.

(12) Wu, S.; Chen, W.; Yan, L., Fabrication of a 3D MnO_2/graphene hydrogel for high-performance asymmetric supercapacitors. *J. Mater. Chem. A* **2014,** *2*, 2765-2772

(13) Sundriyal, P.; Bhattacharya, S., Inkjet-Printed Electrodes on A4 Paper Substrates for Low-Cost, Disposable, and Flexible Asymmetric Supercapacitors. *ACS Appl. Mater. Interfaces* **2017,** *9*, 38507-38521.

(14) Liu, Y.; Miao, X.; Fang, J.; Zhang, X.; Chen, S.; Li, W.; Feng, W.; Chen, Y.; Wang, W.; Zhang, Y., Layered-MnO_2 nanosheet grown on nitrogen-doped graphene template as a composite cathode for flexible solid-state asymmetric supercapacitor. *ACS Appl. Mater. Interfaces* **2016,** *8*, 5251-5260.